APL Materials

Stress engineering of boron doped diamond thin films via micro-fabrication

Fabio Isa, James P. Best, Anna Marzegalli, Marco Albani, Christophe Comte, Jamie J. Kruzic, and Avi Bendavid

View Online   Export Citation   CrossMark

APL Materials
SPECIAL TOPIC: Materials Challenges for Nonvolatile Memory

Submit Today!

Stress engineering of boron doped diamond thin films via micro-fabrication

View Online   Export Citation   CrossMark

Fabio Isa,[1,2,a)] (iD) James P. Best,[3,4] (iD) Anna Marzegalli,[5] (iD) Marco Albani,[6] (iD) Christophe Comte,[1]
Jamie J. Kruzic,[3] (iD) and Avi Bendavid[1,7] (iD)

AFFILIATIONS

[1] CSIRO Manufacturing, 36 Bradfield Road, Lindfield, New South Wales 2070, Australia

[2] Department of Physics and Astronomy, Macquarie University, Sydney, New South Wales 2109, Australia

[3] School of Mechanical and Manufacturing Engineering, University of New South Wales (UNSW Sydney), Sydney, NSW 2052, Australia

[4] Max-Planck-Institut für Eisenforschung GmbH, Max-Planck-Straße 1, D-40237 Düsseldorf, Germany

[5] L-NESS and Dipartimento di Fisica, Politecnico di Milano, via Anzani 42, 22100 Como, Italy

[6] L-NESS and Department of Materials Science, Università di Milano-Bicocca, via Cozzi 55, 20125 Milano, Italy

[7] School of Materials Science and Engineering, University of New South Wales (UNSW, Sydney), Sydney, NSW 2052, Australia

a)**Current address:** Evatec AG, Hauptstrasse 1A, 9477 Trübbach, Switzerland. **Author to whom correspondence should be addressed:** fabio_isa@outlook.com

ABSTRACT

In this paper, a novel approach is presented to tailor the stress properties of diamond thin films via boron doping and micro-fabrication of bridges using focused ion beam milling. The experimental data, based on detailed confocal micro-Raman investigations, are supported and interpreted through finite element method calculations of the stress distribution at mechanical equilibrium. These results indicate that appropriate design of microbridge geometries, together with boron doping, would allow the material stress to be largely enhanced or diminished compared to non-patterned thin films. Our approach, together with a deterministic incorporation and positioning of diamond color centers, may open novel opportunities to tailor the optical and spin properties of diamond-based quantum devices through stress engineering.

Diamond has incredible potential for functional utilization in optical, photonic, and electronic devices based on its high conductivity and chemical inertness while remaining optically transparent.[1,2] With some mechanical properties (e.g., hardness and elastic modulus) reach the limits of known materials, mechanical alteration (i.e., machining) of diamond is a constant challenge. While deposition of diamond-based thin films circumvents several bulk-scale fabrication hurdles, tuning the mechanical strain state with the corresponding properties of diamond layers remains non-trivial. Precise control of the strain in diamond thin films would be of paramount importance to tune the resonance frequency and quality factor of micro-resonators.[3] Focused ion beam (FIB) milling has been utilized to further manipulate diamond coatings to fabricate single-crystal diamond micro-cantilevers[4] and MEMS[5] for sensing applications.

When using top-down micro-fabrication approaches for silicon and germanium, the production of strain enhanced microbridge (MB) structures has been demonstrated as effective in enhancing the material properties.[6,7] Indeed, such solutions can improve the opto-electronic properties of semiconductors, tuning the nature of the material bandgap and enabling the fabrication of group-IV integrated lasers on silicon.[8,9]

Additionally, boron doping of diamond (boron-doped diamond, BDD) can lead to advantageous semi- or super-conducting properties, together with the traditional benefits of diamond, making it attractive for sensing applications in challenging environments.[10] Previously, electron-beam lithography has been used to nanopattern BDD to investigate the robustness of its superconducting properties.[11] However, further developments are needed to capitalize on these concepts of strain

enhancement and boron doping when producing practical diamond structures.

Accordingly, in this paper, we present a novel method of controlling the stress in diamond layers by means of epitaxial growth of a stressed BDD layer, together with FIB milling microbridge structure fabrication. This approach exploits first the biaxial stress generated in the BDD layer due to the different lattice and thermal expansion coefficients[12] compared to the intrinsic diamond substrate.[13–15] Second, two MBs with specific geometries are fabricated, enhancing or reducing the initial stress to reach the mechanical equilibrium condition. The non-homogeneous stress distribution results in a variation of the phonon resonance energy, which is measured by the spectral position change in the diamond Raman peak.[16] The experimental results are corroborated by finite element method (FEM) calculations, which elucidate the stress enhancement/relaxation process induced by the two different MB geometries (hereafter termed as MB1 and MB2).

The samples consisted of two BDD thin films grown by microwave chemical vapor deposition epitaxy on (001) diamond single crystals (see the supplementary material). The BDD thickness for MB1 was 500 nm and for MB2 was 750 nm, while the B concentration in both BDD layers (H terminated surface) was determined from four-point probe I–V curves,[17,18] resulting in a resistivity of 10 mΩ cm, which indicated [B] = 0.8 at. %.

The FIB milled (see the supplementary material) MBs were undercut an angle between the [001] crystal direction and the Ga$^+$ beam of 45°, resulting in wedge-shaped MBs with a bottom surface free of substrate contact. Final polishing with lower currents was performed to achieve the final geometry, as indicated in Fig. 1(a), for MB1.

The stress distribution in the MBs was analyzed by scanning confocal Raman microscopy using a Renishaw inVia spectrometer equipped with a 514 nm laser and a 50× objective with NA = 0.9. The laser spot was focused on the BDD surface, and the lateral and depth resolutions were $(1.22 \times \lambda)/(2 \times \text{NA})$ ∼ 350 nm and λ/NA^2 ∼ 630 nm, respectively. The sample was scanned along the $x//[100] − y//[010]$ directions by means of a piezo-stage in steps of 100 nm, covering an area of at least $40 \times 10\ \mu m^2$. At each $x–y$ position, a Raman spectrum was acquired between 1200 and 1800 cm^{-1}. The diamond Raman peak centered at ω (ω_D = 1332 cm^{-1} for fully relaxed diamond)[19,20] was then fit using a Lorentzian function L, as given in the following equation, where γ is the peak width, a and b are the intensity and offset constants, respectively:

$$L = a \times \gamma/[(\omega − \omega_D)^2 + \gamma^2] + b. \quad (1)$$

The spectral position of the Raman peak is influenced by the stress $\sigma_{xx} + \sigma_{yy}$ distribution in the BDD thin layer[16] according to Eq. (2), while the stress component σ_{zz} along z is relaxed through the (001) free surface, as given in Eq. (3) (for more details, see the chapter "stress–Raman model" in the supplementary material),

$$\sigma_{xx} + \sigma_{yy} = 1.21(\text{GPa/cm}^{-1}) \times (\omega_D − \omega), \quad (2)$$

$$\sigma_{zz} = 0. \quad (3)$$

The spectrometer was equipped with a rotating $\lambda/2$ waveplate (angle θ in 3° steps) on the laser beam and a polarizer on the scattered
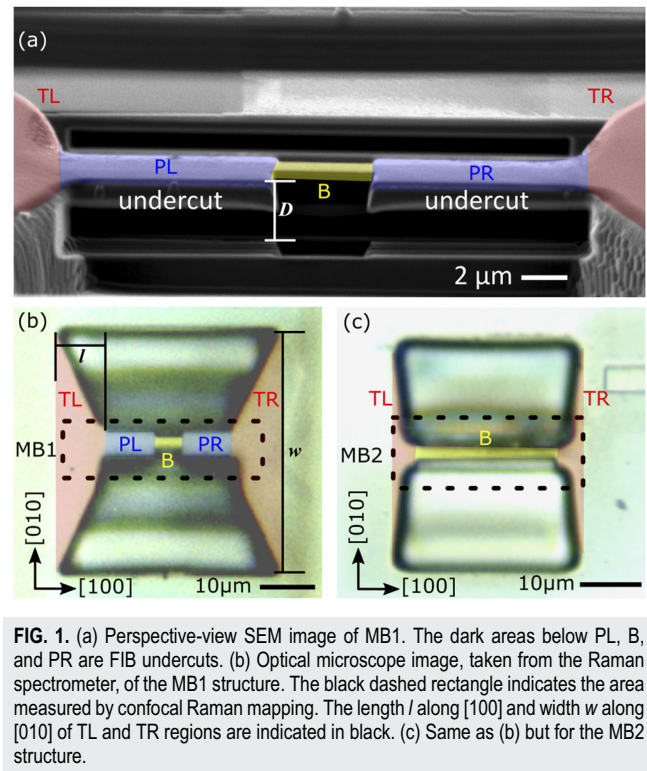
FIG. 1. (a) Perspective-view SEM image of MB1. The dark areas below PL, B, and PR are FIB undercuts. (b) Optical microscope image, taken from the Raman spectrometer, of the MB1 structure. The black dashed rectangle indicates the area measured by confocal Raman mapping. The length l along [100] and width w along [010] of TL and TR regions are indicated in black. (c) Same as (b) but for the MB2 structure.

light to confirm the single-crystal nature of the deposited diamond material.

The geometries of MB1 and MB2 structures are depicted in the perspective-view SEM and optical microscope images shown in Fig. 1. MB1 consists of five different regions marked as left triangular pad (TL—red), left pad (PL—blue), bridge (B—yellow), right pad (PD—blue), and right triangular pad (TR—red). In contrast, MB2 consisted of only three regions: triangular pad (TL—red), bridge (B—yellow), and right triangular pad (TR—red). The dark trapezoidal areas above and below the bridges are undercut materials by FIB milling. The trapezoidal shape was required to efficiently sputter the material and avoid re-deposition during the FIB milling process. The black dashed rectangles in (b) and (c) indicate the area mapped by confocal Raman. Table I reports the length l along [100], width w along [010] [see Fig. 1(a)], and thickness h along [001] of the different MB regions.

Confocal Raman spectra were then taken from the regions highlighted with black dashed rectangles in Figs. 1(b) and 1(c). Figure 2(a) reports in blue the Raman spectrum, obtained in the center of the MB1–TR region. It is dominated by the first order Raman line of diamond.[21] The inset shows the Lorentzian fit function L (orange) of the diamond Raman peak (blue) in the spectral range between 1320 and 1345 cm^{-1}. Notably, the sp^2 carbon Raman signal at higher wavenumbers is negligible, indicating the good crystal quality of the epitaxial diamond.[22] Analogous results were obtained across all the MB1 and MB2 regions. The fit error on the peak position was about 0.2 cm^{-1}, corresponding to a stress uncertainty of 0.07 GPa.

TABLE I. List of MB1 and MB2 geometrical parameters (see Fig. 1) used also in FEM calculations. l is the region length along [100], w is the width along [010], and h is the thickness along [001].

Microbridge	Region	l (μm)	w (μm)	h (μm)
MB1	TL	5.7	17	
MB1	PL	9.5	5.1	2.6
MB1	B	4.3	1.7	0.9
MB1	PR	9.5	5.1	2.6
MB1	TR	5.7	17	
MB2	TL	2.2	12.1	
MB2	B	17.6	1.3	0.7
MB2	TR	2.2	12.1	

For backscattering confocal Raman spectroscopy with the laser beam parallel to the [001] diamond direction and a polarizer on the scattered beam parallel to [100], the Raman selection rules for single crystals[23] indicate that the scattered intensity is proportional to $\sin^2\theta$, where θ is the angle between the laser polarization vector and [100]. Figure 2(b) reports the variation of the diamond Raman integrated intensity, as a function of the laser polarization angle θ, measured in the center of the MB1–TR region. This result confirms the good epitaxial crystal quality of the BDD layer.
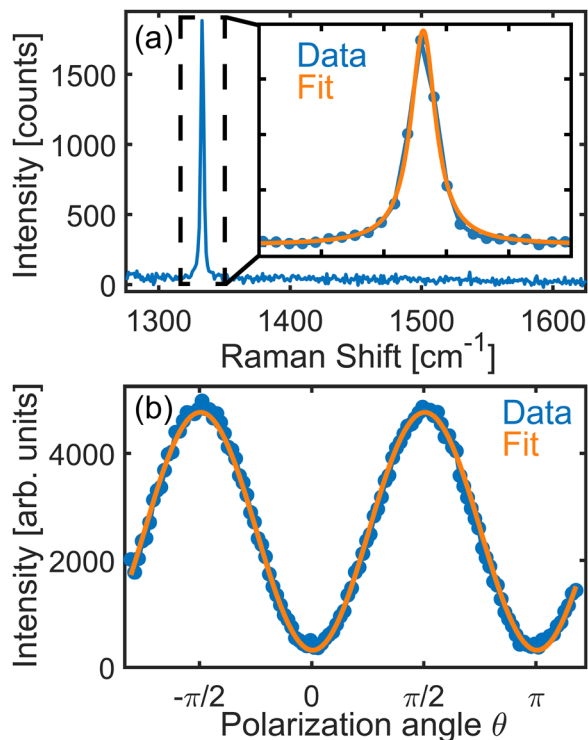
FIG. 2. (a) Raman spectrum obtained from confocal spectroscopy in the center of the MB1–TR region. The inset shows a magnification (black dashed rectangle) of the experimental data (blue) and Lorentzian fit curve L (orange) in the spectral range between 1320 and 1345 cm^{-1}. (b) Integrated intensity of the diamond Raman peak (blue) and its angular fit (orange) as a function of the laser beam polarization angle θ recorded in the center of the MB1–TR region.

Indeed, the angular fit proportional to $\sin^2\theta$ (orange) matches very well with the integrated intensity of the diamond Raman peak (blue) measured at different values of θ, indicating the absence of crystal twins.[19] The same analysis was also performed in the center of each region (TL, PL, PR, and B) of the MB1 and MB2 structures, resulting in similar conclusions.

The stress $\sigma_{xx} + \sigma_{yy}$ was calculated by applying Eqs. (1) and (2) to the Raman spectra obtained by confocal mapping. Importantly, $\sigma_{xx} + \sigma_{yy}$ was also measured in the non-patterned areas about 50 μm away from the MBs, as indicated in Fig. S1. In the non-patterned areas, $\sigma_{xx} + \sigma_{yy}$ average values of 1.49 ± 0.04 and 1.70 ± 0.04 GPa were determined for the MB1 and MB2 samples, respectively (see the supplementary material). The stress variation between the two samples may be ascribed to the different BDD film thicknesses of 500 and 750 nm for the MB1 and MB2 structures, which have a relevant impact on the relaxation of the lattice and thermal mismatch developed during epitaxy and sample cooling to room temperature.[24]

Figure 3(a) shows the distribution of $\sigma_{xx} + \sigma_{yy}$ measured in the MB1 black dashed area marked in Fig. 1(b). The stress variation in each MB1 region is displayed as histograms in Fig. 3(b) for TL, (c) for PL, (d) for B, (e) for PR, and (f) for TR regions.

First, the measured stress distribution is symmetric with respect to the bridge center as a direct consequence of the micro-fabrication geometry. Second, the stress varies significantly in each MB1 region compared to the average value of 1.49 GPa in the non-patterned area. It increases in B, reaching a maximum value of 1.74 GPa and an average value of 1.56 ± 0.09 GPa, and it decreases in PL and PR to 0.96 ± 0.07 GPa and reaches an intermediate value of 1.35 ± 0.03 GPa in TL and TR. The elastic mechanism leading to the non-uniform stress distribution in the MB structure was elucidated by FEM simulations and will be discussed later in this work.

Analogously, Fig. 4(a) reports the stress $\sigma_{xx} + \sigma_{yy}$ distribution of MB2, measured in the black dashed rectangle highlighted in Fig. 1(c). As previously described, the geometry of MB2 differs from that of MB1 due to the lack of the rectangular pads PL and PR. The different geometric structure had a strong impact on the $\sigma_{xx} + \sigma_{yy}$ distribution compared to the results of MB1 presented in Fig. 3. As indicated in the $\sigma_{xx} + \sigma_{yy}$ stress histograms shown in Figs. 4(b)–4(d), while TL and TR areas had only slightly lower average stress compared to the non-patterned region (1.70 GPa), being 1.53 ± 0.07 and 1.56 ± 0.04 GPa, respectively, the stress in region B was significantly reduced to 1.31 ± 0.04 GPa. These results clearly indicate that the stress in BDD/diamond layers can be enhanced or reduced by the appropriate choice of microbridge geometry.
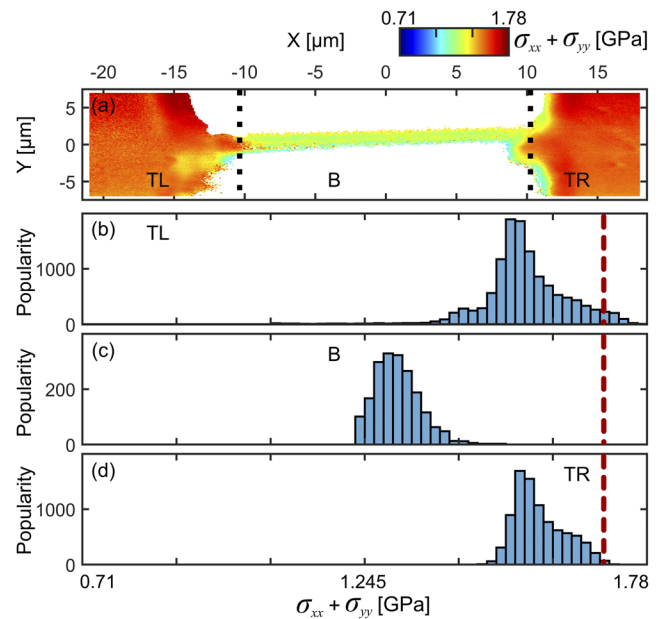
The mechanisms leading to the experimental results reported in Figs. 3 and 4 were elucidated by three-dimensional (3D) FEM simulations as follows: The FEM simulations were performed using the software Comsol Multiphysics. 3D models of the MB structures were implemented using the experimental geometrical parameters reported in Table I. The stress field was calculated by solving the mechanical equilibrium problem, set according to the stress conditions measured by Raman spectroscopy in the non-patterned regions for the BDD layer (see the supplementary material). The equilibrium state was numerically determined by benefitting of the zero-stress condition provided by the free surfaces of the system. The meshes were refined in the MB region where a better resolution of the stress tensor was required [see Figs. S5(a) and S5(d)].
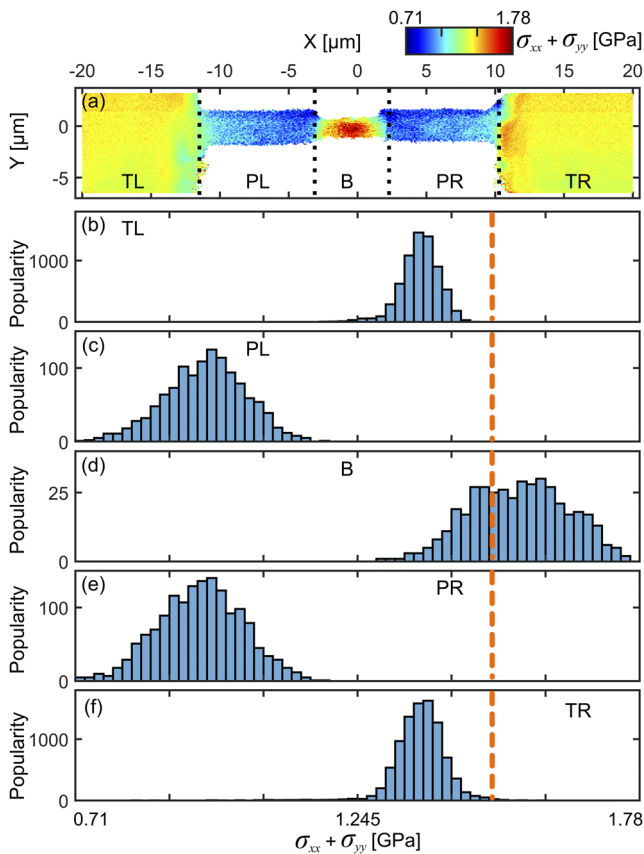
FIG. 3. (a) Color-coded map of the $\sigma_{xx} + \sigma_{yy}$ stress distribution measured from confocal Raman mapping of the MB1 structure. Five different regions, labeled as TL, PL, B, PR, and TR, are separated by black dashed vertical lines. (b) Popularity histogram of the $\sigma_{xx} + \sigma_{yy}$ stress distribution in the TL region. (c)–(f) Same as (b) but for the PL, B, PR, and TR regions, respectively. The histogram bin width is 1.8×10^{-2} GPa, and the orange dashed line represents $\sigma_{xx} + \sigma_{yy}$ in the non-patterned area.

FIG. 4. (a) Color-coded map of the $\sigma_{xx} + \sigma_{yy}$ stress distribution measured from confocal Raman mapping of the MB2 structure. Three different regions, labeled as TL, B, and TR, are indicated with black dashed vertical lines. (b) Popularity histogram of the $\sigma_{xx} + \sigma_{yy}$ stress distribution in the TL region. (c) and (d) Same as (b) but for the B and TR regions, respectively. The histogram bin width is 1.8×10^{-2} GPa, and the dark-red dashed line represents $\sigma_{xx} + \sigma_{yy}$ in the non-patterned area.

The lattice parameter and elastic constants of diamond and BDD were taken from previously published results.[13–15]

The FEM simulations reported in Figs. 5(a) and 5(d) qualitatively resemble and corroborate the experimental $\sigma_{xx} + \sigma_{yy}$ results of MB1 and MB2 reported in Figs. 3 and 4, respectively. Indeed, Fig. 5(a) reports the $\sigma_{xx} + \sigma_{yy}$ color map of MB1: compared to the non-patterned area, $\sigma_{xx} + \sigma_{yy}$ is (i) significantly enhanced within the thin microbridge region B, (ii) strongly reduced in the wide PL and PR regions, and (iii) slightly relaxed in the triangular regions TL and TR. The stress distribution in the MB1 regions can be explained as follows: First, the creation of free surfaces by FIB milling allows stress relaxation by lattice bending (see Fig. S5), which is not possible in a non-patterned film. The stress relaxation process is more effective in the rectangular wide PL and PR regions than in the TL and TR areas. Second, the stress, particularly along the $x - [100]$ direction, is efficiently transferred from the wide PL and PR pads to the thinner and smaller volume bridge region B, deforming and bending it (see Fig. S5). This stress transfer process leads to the higher value of stress for region B, as shown in Fig. 5(a). This mechanism is

further elucidated by the color maps for the in-plane ($x - [100]$ and $y - [010]$ directions) σ_{xx} and σ_{yy} components of the stress tensor, as shown in Figs. 5(b) and 5(c), respectively. The σ_{xx} component of the stress is fully concentrated in the thinnest bridge region B, while the orthogonal component σ_{yy} is almost fully relaxed through the free surfaces, thus resulting in uniaxial stress distribution in B. Importantly, the FEM simulations demonstrate that the $\sigma_{xx} + \sigma_{yy}$ stress in the B region of MB1 is significantly higher than the average value in the non-patterned area, proving that this MB configuration can be exploited to locally increase the diamond stress.

Conversely, by changing the geometry of the suspended microbridge from MB1 to MB2, where the wide rectangular pads PL and PR are missing, the stress enhancement effect in the thin bridge region B is lost. Indeed, the MB2 color map of $\sigma_{xx} + \sigma_{yy}$ shown in Fig. 5(d) indicates that the thin bridge B has much lower $\sigma_{xx} + \sigma_{yy}$ with respect to the nearby non-patterned area. Analogously, the TL and TR partially relax their stress due to the free surfaces. This FEM result is in very good agreement with the experimental data reported in Fig. 4. A more detailed examination of the FEM results further reveals the role of the MB2 geometry in the stress relaxation process. By considering the components of the stress tensor for the in-plane directions, namely, σ_{xx} and σ_{yy} along the $x - [100]$ and $y - [010]$ directions, it is observed that not all stress components decrease in the region B with respect to the non-patterned film. Indeed, as shown in Fig. 5(f), the free surfaces normal to the $y - [010]$ and $z - [001]$ (not shown here) directions very efficiently relax the σ_{yy} and σ_{zz} components through lattice bending and contraction along
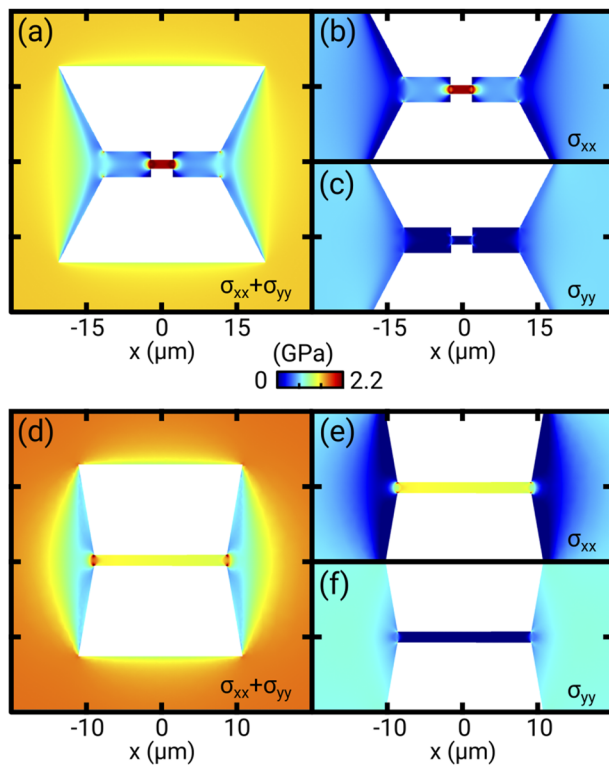
FIG. 5. 3D FEM simulation of the stress distributions for MB1 and MB2 evaluated on the top (001) surface. (a) Top view color-coded map of the calculated $\sigma_{xx} + \sigma_{yy}$ stress, and (b) σ_{xx} and (c) σ_{yy} are the stress components of MB1. (d)–(f) Same as (a)–(c) but for MB2, respectively.

these directions [see Fig. S5(f)]. Contrarily, along the $x - [100]$ direction, there is no equivalent possibility for the MB structure to contract. Indeed, Fig. 5(e) demonstrates that the relaxation process of TL and TR (blue-relaxed regions) results in a high uniaxial stress σ_{xx} value in the thin region B.

By comparing the geometry of MB2 and MB1 structures, it is now clear that the wide rectangular pads PL and PR are necessary for allowing a non-uniform stress relaxation process that enhances the $\sigma_{xx} + \sigma_{yy}$ stress in the thin region B. In contrast, we demonstrated that the pad-less MB2 geometry has a significantly reduced $\sigma_{xx} + \sigma_{yy}$ stress in region B.

In conclusion, we have demonstrated that combining boron doping, together with engineered fabrication of suspended microbridges, enables the control of the stress in diamond thin films. The experimental Raman results, supported by FEM calculations, indicate that biaxial $\sigma_{xx} + \sigma_{yy}$ and uniaxial σ_{xx} stress in the microbridge region can be largely enhanced or diminished by appropriate design. Indeed, if large, relaxed pads (PL and PR in MB1) are present at the ends of the bridge, its uniaxial and biaxial stress is largely enhanced compared to the non-patterned films. Conversely, if the large pads are absent (MB2), the bridge relaxes the stress through the free surfaces, resulting in lower stress than the non-patterned film. Our novel approach may pave the way to the fabrication of integrated diamond surface acoustic wave devices[25] or quantum photonic systems based on diamond color centers,[1,26] where precise tuning of the

diamond stress (~0.1 to 0.4 GPa) is beneficial to improve the optical and spin coherence time by controlling the effect of the thermal phonon bath without lowering the operating temperature.[27]

Additional information on substrate preparation and diamond film growth, focus ion beam milling, the stress–Raman model, stress evaluation in the non-patterned film, and finite element method calculations of material stress can be found in the supplementary material.

DATA AVAILABILITY

The data that support the findings of this study are available from the corresponding author upon reasonable request.

REFERENCES

[1]C. Bradac, W. Gao, J. Forneris, M. E. Trusheim, and I. Aharonovich, Nat. Commun. **10**, 5625 (2019).

[2]N. Donato, N. Rouger, J. Pernot, G. Longobardi, and F. Udrea, J. Phys. D: Appl. Phys. **53**, 093001 (2020).

[3]Y. Cao and N. Sepúlveda, Adv. Mater. Interfaces **6**, 1900887 (2019).

[4]B. Z. Kupfer, R. K. Ahmad, A. Zainal, and R. B. Jackman, Diamond Relat. Mater. **19**, 742 (2010).

[5]M. Liao, Funct. Diamond **1**, 29 (2021).

[6]R. A. Minamisawa, M. J. Süess, R. Spolenak, J. Faist, C. David, J. Gobrecht, K. K. Bourdelle, and H. Sigg, Nat. Commun. **3**, 1096 (2012).

[7]M. J. Süess, R. Geiger, R. A. Minamisawa, G. Schiefler, J. Frigerio, D. Chrastina, G. Isella, R. Spolenak, J. Faist, and H. Sigg, Nat. Photonics **7**, 466 (2013).

[8]S. Wirths, R. Geiger, N. von den Driesch, G. Mussler, T. Stoica, S. Mantl, Z. Ikonic, M. Luysberg, S. Chiussi, J. M. Hartmann, H. Sigg, J. Faist, D. Buca, and D. Grützmacher, Nat. Photonics **9**, 88 (2015).

[9]V. Reboud, A. Gassenq, N. Pauc, J. Aubin, L. Milord, Q. M. Thai, M. Bertrand, K. Guilloy, D. Rouchon, J. Rothman, T. Zabel, F. Armand Pilon, H. Sigg, A. Chelnokov, J. M. Hartmann, and V. Calvo, Appl. Phys. Lett. **111**, 092101 (2017).

[10]Y. He, H. Lin, Z. Guo, W. Zhang, H. Li, and W. Huang, Sep. Purif. Technol. **212**, 802 (2019).

[11]E. A. Ekimov, V. A. Sidorov, E. D. Bauer, N. N. Mel'nik, N. J. Curro, J. D. Thompson, and S. M. Stishov, Nature **428**, 542 (2004).

[12]T. Saotome, K. Ohashi, T. Sato, and H. Maeta, J. Phys.: Condens. Matter **10**, 1267 (1998).

[13]V. V. Brazhkin, E. A. Ekimov, A. G. Lyapin, S. V. Popova, A. V. Rakhmanina, S. M. Stishov, V. M. Lebedev, Y. Katayama, and K. Kato, Phys. Rev. B **74**, 140502(R) (2006).

[14]W. L. Wang, M. C. Polo, G. Sánchez, J. Cifre, and J. Esteve, J. Appl. Phys. **80**, 1846 (1996).

[15]T. Wojewoda, P. Achatz, L. Ortéga, F. Omnès, C. Marcenat, E. Bourgeois, X. Blase, F. Jomard, and E. Bustarret, Diamond Relat. Mater. **17**, 1302 (2008).

[16]M. H. Grimsditch, E. Anastassakis, and M. Cardona, Phys. Rev. B **18**, 901 (1978).

[17] P. Ashcheulov, J. Sebera, A. Kovalenko, F. Fendrych, A. Taylor, O. Frank, L. Kavan, I. Kraus, and I. Kratochvílova, Eur. Phys. J. B **86**, 443 (2013).

[18] R. F. Mamin and T. Inushima, Phys. Rev. B **63**, 033201 (2001).

[19] S. Prawer and R. J. Nemanich, Philos. Trans. R. Soc. London, Ser. A **362**, 2537 (2004).

[20] E. J. Di Liscia, F. Álvarez, E. Burgos, E. B. Halac, H. Huck, and M. Reinoso, Mater. Sci. Appl. **04**, 191 (2013).

[21] A. M. Zaitsev, *Optical Properties of Diamond* (Springer Berlin Heidelberg, 2001).

[22] C. Casiraghi, A. Hartschuh, H. Qian, S. Piscanec, C. Georgi, A. Fasoli, K. S. Novoselov, D. M. Basko, and A. C. Ferrari, Nano Lett. **9**, 1433 (2009).

[23] R. Loudon, Adv. Phys. **13**, 423 (1964).

[24] C. V. Falub, M. Meduňa, D. Chrastina, F. Isa, A. Marzegalli, T. Kreiliger, A. G. Taboada, G. Isella, L. Miglio, A. Dommann, and H. Von Känel, Sci. Rep. **3**, 2276 (2013).

[25] D. Munk, M. Katzman, M. Hen, M. Priel, M. Feldberg, T. Sharabani, S. Levy, A. Bergman, and A. Zadok, Nat. Commun. **10**, 4214 (2019).

[26] S. Maity, L. Shao, S. Bogdanović, S. Meesala, Y. I. Sohn, N. Sinclair, B. Pingault, M. Chalupnik, C. Chia, L. Zheng, K. Lai, and M. Lončar, Nat. Commun. **11**, 193 (2020).

[27] Y. I. Sohn, S. Meesala, B. Pingault, H. A. Atikian, J. Holzgrafe, M. Gündoğan, C. Stavrakas, M. J. Stanley, A. Sipahigil, J. Choi, M. Zhang, J. L. Pacheco, J. Abraham, E. Bielejec, M. D. Lukin, M. Atatüre, and M. Lončar, Nat. Commun. **9**, 2012 (2018).